Non-local tensor sparse coding for multi-image super-resolution in magnetic resonance imaging

Clémence Prévost, F Odille

To cite this version:

Clémence Prévost, F Odille. Non-local tensor sparse coding for multi-image super-resolution in magnetic resonance imaging. 2023. hal-04302420

HAL Id: hal-04302420
https://hal.science/hal-04302420v1

Preprint submitted on 23 Nov 2023

Non-local tensor sparse coding for multi-image super-resolution in magnetic resonance imaging

C. Prévost, *Member, IEEE*, F. Odille

***Abstract*—This paper introduces a non-local tensor sparse coding approach for multi-image super-resolution in magnetic resonance imaging. This approach is composed of four steps: (i) non-local clustering of the similar subtensors, (ii) tensor sparse dictionary learning, (iii) tensor sparse coding and (iv) subtensor regularization. Using the Tucker decomposition, the image reconstruction problem is transformed into learning of sparse dictionaries along the three modes and core tensor sparse coding for each cluster, viewed as tensor. With the proposed approach, reconstruction is achieved with only two low-resolution images, which is a major advantage compared to other multi-frame reconstruction techniques. Flexible conditions for exact recovery are provided. This is also a major advantage of the proposed approach, that will facilitate the clinical implementation of our algorithm, allowing physicians to obtain images very quickly after acquisition, with both practical (convergence analysis) and theoretical guarantees (theorems). The experiments on a set of real quality test phantom and brain datasets show the competitive performance of the proposed approach with a significant gain of time compared to other state-of-the-art methods.**

***Index Terms*—magnetic resonance imaging, super-resolution, multi-modality fusion, inverse methods, compressive sensing**

I. INTRODUCTION

Magnetic resonance imaging (MRI) is a versatile medical imaging modality, providing excellent contrast between soft tissues. However, it suffers from a relatively slow acquisition time (on the order of minutes). This limitation prevents the acquisition of 3D high-resolution images. To circumvent this drawback, super-resolution techniques have been proposed [1], [2]. They consist in recovering a 3D high-resolution image from one or several low-resolution observations.

In [3], [4], it has been proposed to recover the high-resolution image from a single observation using deep learning. Single-image super-resolution falls out of the scope of this paper. Instead, multi-frame super-resolution MRI consists of acquiring several complementary observations of the organ of interest, e.g. three orthogonal scans [5]. Each observation has high in-plane resolutions (1 mm or less) in the plane directions, and low resolution in the slice direction (typically 3 to 10 mm).

It was first proposed to solve the super-resolution problem by regularized inversion, including Tikhonov regularization [6], total variation [7] or Beltrami energy regularizers [8]. Constraints on the rank of the matricized images [9] and patch-based regularization methods [10] were also considered, in the context of super-resolution but also recosntruction from undersampled data in MRI, with applications in MR fingerprinting [11], functional MRI [12] or dynamic reconstruction [13]. However, matrix low-rank methods possessed a high computational burden, and failed at preserving the natural tensor format of the observations. Furthermore, no theoretical guarantees for exact reconstruction of the high-resolution images were provided.

Tensor-based reconstruction methods were recently used [14]–[16] for the reconstruction of medical images, see [17] and references therein for considered applications. Tensor methods generally offer theoretical guarantees for exact image recovery under mild conditions.

In a previous work of the authors [18], a novel tensor-based approach for multi-frame super-resolution MRI was proposed. It was based on a coupled low-rank tensor Tucker approximation of three observations in image space. An algorithm with low computational cost, named isometRic Image Reconstruction by COupled Tensor Tucker Approximation (RICOTTA), was introduced. It was assorted with exact reconstruction of the high-resolution 3D image for a variety of multilinear ranks. This work had several limitations. First, the possible range of usable multilinear ranks was restricted, as it led to inversion of a possibly ill-posed matrix in RICOTTA. As a consequence, there existed a tradeoff in the resolutions of the reconstructed image in the plane and slice directions. Second, the computation time of RICOTTA was still very high for large datasets.

A recent work [19] also used the Tucker decomposition. The problem at hand, single-image super-resolution, was different from the multi-image task considered in this paper. The optimization problem also used a non-local low-rank assumption, but under the form of a penalty term in the cost function. Furthermore, no recovery guarantees were provided.

This paper introduces a non-local tensor sparse coding approach for multi-image super-resolution MRI. This approach is composed of four steps: (i) non-local clustering of the similar subtensors, (ii) tensor sparse dictionary learning, (iii) tensor sparse coding and (iv) subtensor regularization. Using the Tucker decomposition, the image reconstruction problem is transformed into learning of sparse dictionaries along the three modes and core tensor sparse coding for each subtensor. Finally, Beltrami regularization on the reconstructed subtensors promotes feature preservation and avoid staircasing artifacts.

Differently from [10], the proposed algorithm allows one to leverage the need for three observations. Reconstruction from only two low-resolution images leads to a significant

The authors thank CPER IT2MP, Région Lorraine and FEDER. This work was partly supported by the ANR project “Chaire IA Sherlock” ANR-20-CHIA-0031-01 hold by P. Chainais, as well as by the national support within the *programme d’investissements d’avenir* ANR-16-IDEX-0004 ULNE and Région HDF.

C. Prévost (contact author) is with Univ. Lille, CNRS, UMR 9189 CRIStAL, 59000 Lille, France (e-mail: firstname.lastname[at]univ-lille.fr).

F. Odille is with Inserm, Université de. Lorraine, U1254 IADI and CHRU Nancy, CIC-IT 1433, 54000 Nancy, France (e-mail: firstname.lastname[at]inserm.fr).

gain of processing time. New conditions for exact recovery of the high-resolution image of interest are provided, with high flexibility offered by the tensor framework. Such conditions were not offered by the matrix framework in [10].

Outline of the manuscript – A preliminary of this work [18], [20] appears in EUSIPCO 2022, presenting the global Tucker-based approach. This paper is organized as follows. Section II introduces the notation, define the Tucker tensor decomposition operations and recalls the model for multi-image super-resolution MRI. Section III recalls the global Tucker-based approach and the RICOTTA algorithm proposed in [18]. Section IV presents the proposed new non-local tensor sparse coding approach and its advantages. Section V contains theorems for exact recovery of the image using our approach. Section VI describes the simulation setup and Section VII presents the experiments on a real quality test phantom and brain datasets.

II. BACKGROUND AND NOTATION

A. Basic notation

The following notation is used [21]: lowercase (a) or uppercase (A) plain font for scalars, boldface lowercase $(\boldsymbol{a})$ for vectors, uppercase boldface $(\mathbf{A})$ for matrices, and calligraphic $(\boldsymbol{\mathcal{A}})$ for tensors. Vectors are, by convention, one-column matrices. The elements of vectors, matrices and tensors are accessed as a_i, $A_{i,j}$ and $\mathcal{A}_{i_1,\ldots,i_N}$, respectively. $\mathbb{R}$ stands for the real line.

For a matrix $\mathbf{A}$, $\mathbf{A}^\mathsf{T}$ denotes its transpose and $\mathbf{A}^\dagger$ its Moore-Penrose pseudoinverse. The notation $\mathbf{I}_M$ is used for the $M \times M$ identity matrix and $\mathbf{0}_{L\times K}$ for the $L \times K$ matrix of zeroes. The symbol $\boxtimes$ stands for the Kronecker product of matrices (in order to distinguish it from the tensor product $\otimes$), and $\odot$ stands for the Khatri-Rao product.

The operator $\operatorname{vec}\{\cdot\}$ denotes the standard column-major vectorization of a tensor or a matrix. Operator $\bullet_p$ denotes contraction on the p-th index of a tensor. When contracted with a matrix, summation is always performed on the second index of the matrix, e.g., $[\boldsymbol{\mathcal{A}} \bullet_1 \mathbf{M}]_{i,j,k} = \sum_\ell \mathcal{A}_{\ell,j,k} M_{i,\ell}$. For a tensor $\boldsymbol{\mathcal{Y}} \in \mathbb{R}^{I\times J\times K}$, its unfoldings along each mode are denoted by $\mathbf{Y}^{(1)} \in \mathbb{R}^{JK\times I}$, $\mathbf{Y}^{(2)} \in \mathbb{R}^{IK\times J}$ and $\mathbf{Y}^{(3)} \in \mathbb{R}^{IJ\times K}$.

B. Tensor multilinear decomposition

This subsection introduces the tensor decomposition that we will use to build our model. The multilinear decomposition factorizes a tensor into a core tensor multiplied along each mode by factor matrices with ranks (R_1, R_2, R_3). For a tensor $\boldsymbol{\mathcal{X}} \in \mathbb{R}^{I\times J\times K}$, one can express its multilinear decomposition as

$$\boldsymbol{\mathcal{X}} = \boldsymbol{\mathcal{G}} \underset{1}{\bullet} \mathbf{U} \underset{2}{\bullet} \mathbf{V} \underset{3}{\bullet} \mathbf{W} = \sum_{pqr} \mathcal{G}_{p,q,r}\, U_{i,p} V_{j,q} W_{k,r}, \qquad (1)$$

where $\boldsymbol{\mathcal{G}} \in \mathbb{R}^{R_1\times R_2\times R_3}$ is called the core tensor of the decomposition. The matrices $\mathbf{U} \in \mathbb{R}^{I\times R_1}$, $\mathbf{V} \in \mathbb{R}^{J\times R_2}$ and $\mathbf{W} \in \mathbb{R}^{K\times R_3}$ are the factors along each mode. The multilinear decomposition can be compactly written as

$$\boldsymbol{\mathcal{X}} = [\![\boldsymbol{\mathcal{G}};\, \mathbf{U}, \mathbf{V}, \mathbf{W}]\!]. \qquad (2)$$

The following equalities hold for tensor unfolding and vectorization:

$$\begin{aligned} \mathbf{X}^{(1)} &= (\mathbf{W} \boxtimes \mathbf{V})\, \mathbf{G}^{(1)} \mathbf{U}^\mathsf{T}, \\ \operatorname{vec}\{\boldsymbol{\mathcal{X}}\} &= (\mathbf{W} \boxtimes \mathbf{V} \boxtimes \mathbf{U}) \operatorname{vec}\{\boldsymbol{\mathcal{G}}\}. \end{aligned}$$

If (R_1, R_2, R_3) are the smallest possible, *i.e.*,

$$R_1 = \operatorname{rank}\{\mathbf{X}^{(1)}\},\ R_2 = \operatorname{rank}\{\mathbf{X}^{(2)}\},\ R_3 = \operatorname{rank}\{\mathbf{X}^{(3)}\}, \quad (3)$$

then Equation (2) is called Tucker decomposition of $\boldsymbol{\mathcal{X}}$ and the triple (R_1, R_2, R_3) is called the multilinear rank.

C. Multi-image super-resolution MRI observation model

Three low-resolution 3D images (LRI) are observed : $\boldsymbol{\mathcal{Y}}_1 \in \mathbb{R}^{x_1\times y\times s}$, $\boldsymbol{\mathcal{Y}}_2 \in \mathbb{R}^{x\times y_2\times s}$ and $\boldsymbol{\mathcal{Y}}_3 \in \mathbb{R}^{x\times y\times s_3}$, respectively. They represent the same object, hence they can be viewed as degraded versions of a high-resolution image $\boldsymbol{\mathcal{X}} \in \mathbb{R}^{x\times y\times s}$. In the MRI framework, usually $x = y = s$ and $\boldsymbol{\mathcal{X}}$ is called a high-resolution isotropic image (HRII). The scalars s, s_3 denote the number of frontal slices, while x, x_1 and y, y_2 stand for the spatial resolution of each slice (resp. horizontally and vertically). Each observation is downsampled in one direction, thus $x_1 \ll x$, $y_2 \ll y$ and $s_3 \ll s$. The ratio of degraded to high-resolution dimensions depend on the machine settings and acquisition sequence. The multi-image super-resolution MRI problem consists in recovering the HRII $\boldsymbol{\mathcal{X}}$ from the LRI $\boldsymbol{\mathcal{Y}}_1$, $\boldsymbol{\mathcal{Y}}_2$ and $\boldsymbol{\mathcal{Y}}_3$.

The following degradation model [18] is adopted:

$$\begin{cases} \boldsymbol{\mathcal{Y}}_1 &= \boldsymbol{\mathcal{X}} \bullet_1 \mathbf{D}_1 + \boldsymbol{\mathcal{E}}_1, \\ \boldsymbol{\mathcal{Y}}_2 &= \boldsymbol{\mathcal{X}} \bullet_2 \mathbf{D}_2 + \boldsymbol{\mathcal{E}}_2, \\ \boldsymbol{\mathcal{Y}}_3 &= \boldsymbol{\mathcal{X}} \bullet_3 \mathbf{D}_3 + \boldsymbol{\mathcal{E}}_3. \end{cases} \qquad (4)$$

The degradation matrices $\mathbf{D}_i$ $(i = 1, 2, 3)$ are downsampling and reweighing matrices such as $\mathbf{D}_1 \in \mathbb{R}^{x_1\times x}$, $\mathbf{D}_2 \in \mathbb{R}^{y_2\times y}$ and $\mathbf{D}_3 \in \mathbb{R}^{s_3\times s}$. The tensors $\boldsymbol{\mathcal{E}}_i$ $(i = 1, 2, 3)$ represent isotropic white Gaussian noise.

III. TUCKER-BASED IMAGE FUSION

In [18] it was proposed to model the HRII data cube as a tensor with low multilinear rank using the Tucker decomposition. Given (R_1, R_2, R_3) the multilinear rank of the HRII $\boldsymbol{\mathcal{X}}$, $\boldsymbol{\mathcal{X}} = [\![\boldsymbol{\mathcal{G}};\, \mathbf{U}, \mathbf{V}, \mathbf{W}]\!]$ was its Tucker decomposition (TD), where $\mathbf{U} \in \mathbb{R}^{x\times R_1}$, $\mathbf{V} \in \mathbb{R}^{y\times R_2}$ and $\mathbf{W} \in \mathbb{R}^{s\times R_3}$ were the factor matrices and $\boldsymbol{\mathcal{G}} \in \mathbb{R}^{R_1\times R_2\times R_3}$ was the core tensor.

The image reconstruction problem was expressed as the following optimization problem:

$$\underset{\widehat{\mathbf{U}}, \widehat{\mathbf{V}}, \widehat{\mathbf{W}}, \widehat{\mathbf{G}}}{\text{minimize}} \quad f_{TD}(\widehat{\mathbf{U}}, \widehat{\mathbf{V}}, \widehat{\mathbf{W}}, \widehat{\mathbf{G}}), \qquad (5)$$

where $f_{TD}(\widehat{\mathbf{U}}, \widehat{\mathbf{V}}, \widehat{\mathbf{W}}, \widehat{\mathbf{G}}) =$

$$\sum_{i=1}^{3} \lambda_i \|\boldsymbol{\mathcal{Y}}_i - [\![\boldsymbol{\mathcal{G}};\, \widehat{\mathbf{U}}, \widehat{\mathbf{V}}, \widehat{\mathbf{W}}]\!] \bullet_i \mathbf{D}_i\|_F^2 + \mu \mathcal{R}([\![\boldsymbol{\mathcal{G}};\, \widehat{\mathbf{U}}, \widehat{\mathbf{V}}, \widehat{\mathbf{W}}]\!]). \quad (6)$$

The scalars λ_i $(i = 1, 2, 3)$ were balance parameters controlling the weights of the LRIs in the cost function. The operator $\mathcal{R}(\cdot)$ was a Tikhonov regularizer [22] on the reconstructed HRII, with a weight controlled by the scalar μ.

Algorithm 1: RICOTTA

```
input : $\boldsymbol{\mathcal{Y}}_1$, $\boldsymbol{\mathcal{Y}}_2$, $\boldsymbol{\mathcal{Y}}_3$, $\mathbf{D}_i$ $(i = 1, 2, 3)$; $R_1, R_2, R_3$
output: Reconstructed HRII $\widehat{\boldsymbol{\mathcal{X}}}$
1 $\widehat{\mathbf{U}} \leftarrow \text{tSVD}_{R_1}\left(\left[\mathbf{Y}_2^{(1)}\ \mathbf{Y}_3^{(1)}\right]\right)$
2 $\widehat{\mathbf{V}} \leftarrow \text{tSVD}_{R_2}\left(\left[\mathbf{Y}_1^{(2)}\ \mathbf{Y}_3^{(2)}\right]\right)$
3 $\widehat{\mathbf{W}} \leftarrow \text{tSVD}_{R_3}\left(\left[\mathbf{Y}_1^{(3)}\ \mathbf{Y}_2^{(3)}\right]\right)$
4 $\widehat{\boldsymbol{\mathcal{G}}} \leftarrow \underset{\boldsymbol{\mathcal{G}}}{\text{argmin}}\ f_{TD}(\widehat{\mathbf{U}}, \widehat{\mathbf{V}}, \widehat{\mathbf{W}}, \widehat{\mathbf{G}})$
5 $\widehat{\boldsymbol{\mathcal{X}}} = [\![\widehat{\boldsymbol{\mathcal{G}}};\ \widehat{\mathbf{U}}, \widehat{\mathbf{V}}, \widehat{\mathbf{W}}]\!]$
```

A closed-form algorithm was proposed as a sub-optimal solution for (5). This approach, called RICOTTA, is summarized in Algorithm 1. Steps 1–3 of RICOTTA estimated the factors $\mathbf{U}$, $\mathbf{V}$, $\mathbf{W}$ by computing the truncated SVD (tSVD) of the unfolding with rank R_1 (resp. R_2, R_3) . Step 4 of RICOTTA consisted in solving a least-squares problem through normal equations viewed as a generalized Sylvester equation. See Appendix A for more details. The total computational complexity of RICOTTA was

- $\mathcal{O}((R_1 + R_2 + R_3)xys)$ flops for Steps 1–3;
- $\mathcal{O}(\min(R_3^3 + (R_1R_2)^3; R_1^3 + (R_2R_3)^3))$ flops for Step 4.

Using RICOTTA led to a tradeoff in the resolutions of the reconstructed image in the plane and slice directions. Indeed, choosing high ranks led to inversion of a possibly ill-posed matrix in Step 4 of RICOTTA [18]. Therefore, in the following section, a new approach, using non-local decompositions, is introduced.

IV. NON-LOCAL TENSOR SPARSE CODING

The four steps of the approach described in this section are summarized in Figure 1.

A. *Exploiting non-local similarities*

Non-local self-similarity is a useful prior for reconstruction of medical images, since the observations often depict similar structures and usually have strong in-slice correlation [10]. In other words, for a given given MRI subtensor, some similar subtensors can be found within the whole image.

The LRI $\boldsymbol{\mathcal{Y}}_3 \in \mathbb{R}^{x \times y \times s_3}$ contains high-resolution in-plane information. Let it be partitioned into $M_x \times M_y$ square overlapping cubes of size $p \times p \times s$, where

$$M_x = \left\lfloor \frac{x-p}{p-o} + 1 \right\rfloor,\ M_y = \left\lfloor \frac{y-p}{p-o} + 1 \right\rfloor, \tag{7}$$

and o is the overlap. The similar subtensors of $\boldsymbol{\mathcal{Y}}_3$ are grouped into K clusters using K-means++ [23]. Each cluster contains at most n_k cubes, $k = \{1, \ldots, K\}$ and can be viewed as a fourth-order tensor.

Each cluster is reshaped into a third-order tensor $\boldsymbol{\mathcal{P}}^k_{\boldsymbol{\mathcal{Y}}_3} \in \mathbb{R}^{p^2 \times s_3 \times n_k}$, $k = \{1, \ldots, K\}$ such that

$$\left(\boldsymbol{\mathcal{P}}^k_{\boldsymbol{\mathcal{Y}}_3}\right)_{:,:,j} = \left(\mathbf{Y}_\mathbf{3}^{\mathbf{k},\mathbf{j}}\right)^{(3)}\ \forall\ j = \{1, \ldots, n_k\}. \tag{8}$$

Each slice of $\boldsymbol{\mathcal{P}}^k_{\boldsymbol{\mathcal{Y}}_3}$ is the matricization of a subtensor of $\boldsymbol{\mathcal{Y}}_3$, denoted $\boldsymbol{\mathcal{Y}}_3^{k,j}$.

Based on the learned cluster structure, clusters with the same spatial structure are built from $\boldsymbol{\mathcal{Y}}_1$ and $\boldsymbol{\mathcal{Y}}_2$. A pixel in $\boldsymbol{\mathcal{Y}}_1$ (resp. $\boldsymbol{\mathcal{Y}}_2$) corresponds to a $d_x \times 1$ (resp. $1 \times d_y$) patch in $\boldsymbol{\mathcal{Y}}_3$, where $d_x = \frac{x}{x_1}$ (resp. $d_y = \frac{y}{y_2}$).

For instance, if any pixel in a $d_x \times 1$ patch of $\boldsymbol{\mathcal{Y}}_3$ belongs to the k-th cluster, the corresponding pixel in in $\boldsymbol{\mathcal{Y}}_1$ is also added to k-th cluster, and likewise for the pixels of $\boldsymbol{\mathcal{Y}}_2$. The pixels in $\boldsymbol{\mathcal{Y}}$ may belong to different clusters, therefore the pixels in $\boldsymbol{\mathcal{Y}}_1$ and $\boldsymbol{\mathcal{Y}}_2$ may also belong to several clusters in parallel. Similarly to Equation (8), the third-order tensors $\boldsymbol{\mathcal{P}}^k_{\boldsymbol{\mathcal{Y}}_1} \in \mathbb{R}^{p \times s \times N_k}$ and $\boldsymbol{\mathcal{P}}^k_{\boldsymbol{\mathcal{Y}}_2} \in \mathbb{R}^{p \times s \times N_k}$ are constructed from the cluster structure obtained from $\boldsymbol{\mathcal{Y}}_1$ and $\boldsymbol{\mathcal{Y}}_2$, where N_k is the number of pixels belonging to the k-th cluster.

B. *Tensor dictionary learning*

Since the subtensors in a same cluster are similar to each other, we assume that they admit a sparse representation. The dictionary learning step is described for the k-th cluster without loss of generality, and the procedure for other clusters is likewise.

Let $\boldsymbol{\mathcal{P}}^k_{\boldsymbol{\mathcal{X}}} \in \mathbb{R}^{p^2 \times s \times n_k}$ denote the third-order tensor constructed from the k-th cluster of $\boldsymbol{\mathcal{X}}$. Let us assume that $\boldsymbol{\mathcal{P}}^k_{\boldsymbol{\mathcal{X}}}$ admits a Tucker decomposition of the form

$$\boldsymbol{\mathcal{P}}^k_{\boldsymbol{\mathcal{X}}} = [\![\boldsymbol{\mathcal{G}}^k;\ \mathbf{U}^k, \mathbf{V}^k, \mathbf{W}^k]\!], \tag{9}$$

where the factor matrices $\mathbf{U}^k \in \mathbb{R}^{p^2 \times R_1^k}$, $\mathbf{V}^k \in \mathbb{R}^{s \times R_2^k}$, $\mathbf{W}^k \in \mathbb{R}^{n_k \times R_3^k}$ are the dictionaries in the three modes with R_1^k (resp. R_2^k, R_3^k) atoms. The core tensor $\boldsymbol{\mathcal{G}}^k \in \mathbb{R}^{R_1^k \times R_2^k \times R_3^k}$ encodes the interactions between the columns of the dictionaries.

Following the model (4), the tensors constructed from $\boldsymbol{\mathcal{Y}}_3$ can be written as

$$\boldsymbol{\mathcal{P}}^k_{\boldsymbol{\mathcal{Y}}_3} = [\![\boldsymbol{\mathcal{G}}^k;\ \mathbf{U}^k, \tilde{\mathbf{V}}^k, \mathbf{W}^k]\!], \tag{10}$$

where $\tilde{\mathbf{V}}^k = \mathbf{D}_3\mathbf{V}^k \in \mathbb{R}^{s_3 \times R_2^k}$ is the dictionary containing the degraded information in the slice dimension. From Equation (10), $\boldsymbol{\mathcal{P}}^k_{\boldsymbol{\mathcal{Y}}_3}$ contains the same high-resolution information in the plane and cluster dimensions as in $\boldsymbol{\mathcal{P}}^k_{\boldsymbol{\mathcal{X}}}$. Therefore the dictionaries $\mathbf{U}^k$ and $\mathbf{W}^k$ can be extracted from $\boldsymbol{\mathcal{P}}^k_{\boldsymbol{\mathcal{Y}}_3}$.

Unfolding $\boldsymbol{\mathcal{P}}^k_{\boldsymbol{\mathcal{Y}}_3}$ in Equation (10) along the first mode yields

$$\left(\mathbf{P}^{\mathbf{k}}_{\boldsymbol{\mathcal{Y}}_\mathbf{3}}\right)^{(1)} = \mathbf{A}^k_{\boldsymbol{\mathcal{Y}}_3}\left(\mathbf{U}^k\right)^\intercal, \tag{11}$$

where $\mathbf{A}^k_{\boldsymbol{\mathcal{Y}}_3} = \left(\mathbf{W}^k \boxtimes \tilde{\mathbf{V}}^k\right)\left(\mathbf{G}^k\right)^{(1)}$. In Equation (11), the rows of $\left(\mathbf{P}^{\mathbf{k}}_{\boldsymbol{\mathcal{Y}}_\mathbf{3}}\right)^{(3)}$ can be written as a linear combination of rows of $\mathbf{U}^k$. However, estimation of $\mathbf{U}^k$ is severely ill-posed, because $\mathbf{A}^k_{\boldsymbol{\mathcal{Y}}_3}$ is non-unique.

To regularize this problem, a sparsity-inducing prior is used. As a by-product, it promotes the sparsity of the core tensor $\boldsymbol{\mathcal{G}}^k$. Hence estimation of $\mathbf{U}^k$ can be viewed as sparse dictionary learning as follows:

$$\min_{\mathbf{A}^k_{\boldsymbol{\mathcal{Y}}_3}, \mathbf{U}^k} \ \|\left(\mathbf{P}^{\mathbf{k}}_{\boldsymbol{\mathcal{Y}}_\mathbf{3}}\right)^{(1)} - \mathbf{A}^k_{\boldsymbol{\mathcal{Y}}_3}\left(\mathbf{U}^k\right)^\intercal\|_F^2, \tag{12}$$

$$\text{s. t. } \|\mathbf{A}^k_{\boldsymbol{\mathcal{Y}}_3}(\ell, :)\|_0 \leqslant \epsilon_u \text{ for } 1 \leqslant \ell \leqslant s_3 n_k, \tag{13}$$

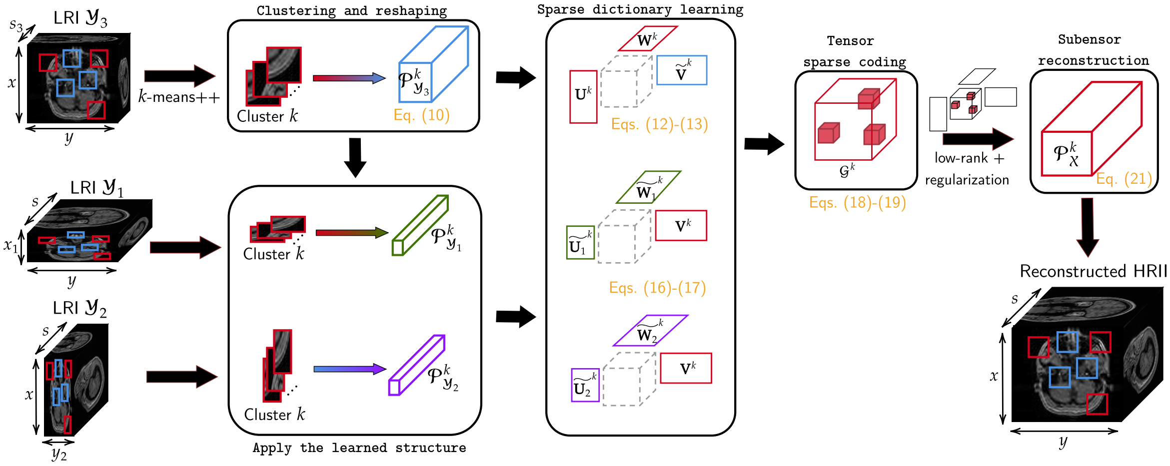

Fig. 1. Pipeline of the proposed approach.

where $\|\cdot\|_F$ and $\|\cdot\|_0$ respectively denote the Frobenius norm and the ℓ_0 norm, and ϵ_u is the maximum possible number of non-zero elements in the ℓ-th row of $\mathbf{A}^k_{\boldsymbol{\mathcal{Y}}_3}$. To solve the problem (12) under constraints (13), the dictionary-updates-cycles K-SVD (DUC-KSVD) [24] approach is employed.

Estimation of $\mathbf{W}^k$ can also be performed from $\boldsymbol{\mathcal{P}}^k_{\boldsymbol{\mathcal{Y}}_3}$ by unfolding Equation (10) along the third mode, and solved using DUC-KSVD.

The subtensors constructed from $\boldsymbol{\mathcal{Y}}_1$ and $\boldsymbol{\mathcal{Y}}_2$ are written as

$$\boldsymbol{\mathcal{P}}^k_{\boldsymbol{\mathcal{Y}}_1} = \llbracket \boldsymbol{\mathcal{G}}^k;\, \widetilde{\mathbf{U}}^k_1, \mathbf{V}^k, \widetilde{\mathbf{W}}^k_1 \rrbracket,\ \boldsymbol{\mathcal{P}}^k_{\boldsymbol{\mathcal{Y}}_2} = \llbracket \boldsymbol{\mathcal{G}}^k;\, \widetilde{\mathbf{U}}^k_2, \mathbf{V}^k, \widetilde{\mathbf{W}}^k_2 \rrbracket \tag{14}$$

where the matrices $\widetilde{\mathbf{W}}^k_1 \in \mathbb{R}^{N_K \times R^k_3}$ and $\widetilde{\mathbf{W}}^k_2 \in \mathbb{R}^{N_K \times R^k_3}$ encode the learned cluster structure applied to $\boldsymbol{\mathcal{Y}}_1$ and $\boldsymbol{\mathcal{Y}}_2$. The matrices $\widetilde{\mathbf{U}}^k_1 \in \mathbb{R}^{p \times R^k_1}$ and $\widetilde{\mathbf{U}}^k_2 \in \mathbb{R}^{p \times R^k_3}$ contain the degraded in-plane information in the subtensors of $\boldsymbol{\mathcal{Y}}_1$ and $\boldsymbol{\mathcal{Y}}_2$.

Conversely, $\boldsymbol{\mathcal{P}}^k_{\boldsymbol{\mathcal{Y}}_1}$ and $\boldsymbol{\mathcal{P}}^k_{\boldsymbol{\mathcal{Y}}_2}$ contain the same high-resolution in-slice information, encoded in the matrix $\mathbf{V}^k \in \mathbb{R}^{s \times R^k_2}$. As a result, since the two observations have similar noise contaminations, estimation of $\mathbf{V}^k$ can be performed from only one observation $\boldsymbol{\mathcal{Y}}_1$ or $\boldsymbol{\mathcal{Y}}_2$ (in the case where the two observations have different resolutions, the observation with the highest in-plane resolution should be preferred). In the rest of this subsection, the dictionary learning process for $\mathbf{V}^k$ is described using only $\boldsymbol{\mathcal{P}}^k_{\boldsymbol{\mathcal{Y}}_1}$, and estimation from $\boldsymbol{\mathcal{P}}^k_{\boldsymbol{\mathcal{Y}}_2}$ can be performed in a similar fashion.

Since subtensors of $\boldsymbol{\mathcal{Y}}_1$ can be related to several clusters simultaneously, the relationship between $\widetilde{\mathbf{U}}^k_1$ and $\mathbf{U}^k$ is highly complex. Therefore, in this paper, the coupling relationships between those matrices is ignored, resulting in a versatile, semi-blind approach. From Equation (14),

$$\left(\mathbf{P}^{\mathbf{k}}_{\boldsymbol{\mathcal{Y}}_1}\right)^{(2)} = \mathbf{C}^k_{\boldsymbol{\mathcal{Y}}_1} \left(\mathbf{V}^k\right)^{\mathsf{T}}, \tag{15}$$

where $\mathbf{C}^k_{\boldsymbol{\mathcal{Y}}_1} = \left(\widetilde{\mathbf{W}}^k_1 \boxtimes \widetilde{\mathbf{U}}^k_1\right)\left(\mathbf{G}^k\right)^{(2)}$.

Sparsity-constrained dictionary-learning is used to estimate the $\mathbf{W}^k$ dictionaries:

$$\min_{\mathbf{C}^k_{\boldsymbol{\mathcal{Y}}_1}, \mathbf{V}^k} \left\| \left(\mathbf{P}^{\mathbf{k}}_{\boldsymbol{\mathcal{Y}}_1}\right)^{(2)} - \mathbf{C}^k_{\boldsymbol{\mathcal{Y}}_1} \left(\mathbf{V}^k\right)^{\mathsf{T}} \right\|^2_F, \tag{16}$$

$$\text{s. t. } \|\mathbf{C}^k_{\boldsymbol{\mathcal{Y}}_1}(\ell, :)\|_0 \leqslant \epsilon_v,\ \text{ for } 1 \leqslant \ell \leqslant pN_k, \tag{17}$$

where ϵ_v is the maximum sparsity. The problem (16) under constraints (17) is also solved using DUC-KSVD.

C. Tensor sparse coding

Once the dictionaries $\mathbf{U}^k, \mathbf{V}^k, \mathbf{W}^k$ have been retrieved for the k-th cluster, the core tensor $\boldsymbol{\mathcal{G}}^k$ must be estimated. Since the estimated dictionaries are sparse, we assume that they are redundant enough to represent the subtensors of the HRII, which induces sparsity of the core tensor $\boldsymbol{\mathcal{G}}^k$. Estimation of the core tensor can be performed by solving the following sparse optimization problem:

$$\min_{\boldsymbol{\mathcal{G}}^k} \|\boldsymbol{\mathcal{P}}^k_{\boldsymbol{\mathcal{Y}}_3} - \llbracket \boldsymbol{\mathcal{G}}^k;\, \mathbf{U}^k, \mathbf{D}_3\mathbf{V}^k, \mathbf{W}^k \rrbracket\|^2_F, \tag{18}$$

$$\text{s. t. } \|\boldsymbol{\mathcal{G}}^k\|_0 \leqslant \epsilon_g, \tag{19}$$

where ϵ_g is the maximum admissible sparsity.

The above problem can be reformulated by vectorizing (18) by exploiting the relationship between vectorization and Kronecker product, yielding the equivalent problem

$$\begin{aligned} \min_{\boldsymbol{\mathcal{G}}^k} \|\, &\mathrm{vec}\{\llbracket \boldsymbol{\mathcal{P}}^k_{\boldsymbol{\mathcal{Y}}_3};\, \mathbf{U}^{k\mathsf{T}}, \mathbf{V}^{k\mathsf{T}}\mathbf{D}^{\mathsf{T}}_3, \mathbf{W}^{k\mathsf{T}} \rrbracket\} \\ &- \left(\mathbf{I}_{R^k_3} \boxtimes \mathbf{V}^{k\mathsf{T}}\mathbf{D}^{\mathsf{T}}_3\mathbf{D}_3\mathbf{V}^k \boxtimes \mathbf{I}_{R^k_1}\right)\boldsymbol{g}^k\|^2_F, \end{aligned} \tag{20}$$

where $\boldsymbol{g}^k$ is the standard vectorization of the core tensor.

Since problem (20) under constraints (19) is NP-hard [25], we solve it by using the greedy Matching Pursuit Lasso (MPL) [26]. This method is based on quadratically constrained linear programing, which greatly reduces the computation cost of the sparse coding problem over large dictionaries.

D. Subtensor reconstruction

Once the dictionaries $\mathbf{U}^k, \mathbf{V}^k, \mathbf{W}^k$ and the core tensor $\boldsymbol{\mathcal{G}}^k$ have been estimated, the corresponding subtensor of $\boldsymbol{\mathcal{X}}$ can be reconstructed by solving the following Beltrami-regularized problem:

$$\begin{aligned} \boldsymbol{\mathcal{P}}^k_{\boldsymbol{\mathcal{X}}} = \operatorname*{argmin}_{\boldsymbol{\mathcal{I}}} &\int \sqrt{1 + \beta^2 |\nabla \boldsymbol{\mathcal{I}}|^2} \\ &+ \frac{\rho}{2} \int \|\boldsymbol{\mathcal{I}} - \llbracket \boldsymbol{\mathcal{G}}^k;\, \mathbf{U}^k, \mathbf{V}^k, \mathbf{W}^k \rrbracket\|^2_F, \end{aligned} \tag{21}$$

where $\beta, \rho > 0$ are balance parameters. In practice, Equation (21) is solved using a primal-dual projected gradients optimization algorithm, described in details in [27].

Then, the subtensors of the HRII are returned to their location by straight averaging. The proposed algorithm is summarized in Algorithm (2).

Algorithm 2: Proposed algorithm

```
input : Observations $\boldsymbol{\mathcal{Y}}_i$, degradation matrix $\mathbf{D}_3$; parameters
        $p, K, (R_1^k, R_2^k, R_3^k), \epsilon_u, \epsilon_v, \epsilon_w, \epsilon_g$.
output: A non-local low-rank approximation $\widehat{\boldsymbol{\mathcal{X}}}$ of $\boldsymbol{\mathcal{X}}$.
1 for $k = 1, \ldots, K$ do
2     Estimate $\mathbf{U}^k, \mathbf{V}^k, \mathbf{W}^k$ by solving Problems (12) to (17)
3     Estimate $\boldsymbol{\mathcal{G}}^k$ by solving (20) under constraints (19)
4 end
5 Reconstruct subtensors of $\widehat{\boldsymbol{\mathcal{X}}}$ using Equation (21)
```

Complexity – Steps 2 to 4 in Algorithm 2 are dominated by the cost of the SVD in the DUC-KSVD algorithms. The cost of the tensor sparse coding step is dominated by that of the worst case analysis in the MPL algorithm. Therefore, the total cost for Algorithm 2 per cluster is

- $\mathcal{O}\left(R_1^k p^4 s_3 n_k\right)$ for Step 2;
- $\mathcal{O}\left(R_2^k p^2 s_3 n_k^2\right)$ for Step 3;
- $\mathcal{O}\left(R_3^k p^2 s^2 n_k\right)$ for Step 4;
- $\mathcal{O}(\prod_j R_j^k p^2 s_3 n_k)$ for Step 5.

Convergence – By [26, Theorems 2 and 3], MPL linearly converges to an optimal solution of Problem (20)–(19). Under the condition that the sparse coding stage can be performed exactly, KSVD is also guaranteed to converge to a local minimum for estimation of the dictionaries [24].

Reconstruction from only two observations – Estimation of $\mathbf{V}^k$ can be performed from either $\boldsymbol{\mathcal{P}}_{\boldsymbol{\mathcal{Y}}_1}^k$ or $\boldsymbol{\mathcal{P}}_{\boldsymbol{\mathcal{Y}}_2}^k$ similarly without loss of performance. In other words, only two LRI are required to solve the reconstruction problem.

Semi-blind reconstruction – Since the relationship between $\widetilde{\mathbf{U}}_1^k$ (resp. $\widetilde{\mathbf{U}}_2^k$) is highly complex, we chose not to model it when solving for the dictionaries. In practice, it means that the proposed approach only requires knowledge of the degradation matrix $\mathbf{D}_3$ in model (4), therefore it can be referred to as semi-blind.

Remark – For $p \leqslant x$ and $M_x, M_y > 1$, if each cluster of $\boldsymbol{\mathcal{Y}}_3$ is reshaped into a matrix $\mathbf{P}_{\boldsymbol{\mathcal{Y}}_3}^k \in \mathbb{R}^{p^2 s_3 \times n_k}$, *i.e.*,

$$\left(\mathbf{P}_{\boldsymbol{\mathcal{Y}}_3}^k\right)_{:,j} = \operatorname{vec}\{Y_3^{k,j}\} \ \forall \ j = \{1, \ldots, n_k\}, \tag{22}$$

then solving the reconstruction problem becomes matrix-based. It can then be solved using the method proposed in [10], that also considers sparse coding but uses an Augmented Lagrangian formulation with high computational burden.

V. RECOVERY OF THE HIGH-RESOLUTION ISOTROPIC IMAGE

This section provides conditions for exact reconstruction of the HRII tensor. Although the Tucker decomposition is not unique, the proposed approach still recovers the subtensors of the HRII uniquely.

A. Deterministic exact recovery

The following theorems address exact recovery of the k-th subtensor of $\boldsymbol{\mathcal{X}}$, and the proof for the other subtensors can be obtained analogously.

Theorem V.1. *Let $\boldsymbol{\mathcal{P}}_{\boldsymbol{\mathcal{X}}}^k$ admit a Tucker decomposition as in Equation* (9) *where $\mathbf{U}^k \in \mathbb{R}^{p^2 \times R_1^k}, \mathbf{V}^k \in \mathbb{R}^{s \times R_2^k}, \mathbf{W}^k \in \mathbb{R}^{n_k \times R_3^k}$ have full column rank. We also assume that $\boldsymbol{\mathcal{E}}_i = \mathbf{0}$ $(i = 1, 2, 3)$ in* (4). *If*

$$\operatorname{rank}\{(\mathbf{P}_{\boldsymbol{\mathcal{Y}}_3}^{\mathbf{k}})^{(1)}\} = R_1^k, \ \operatorname{rank}\{(\mathbf{P}_{\boldsymbol{\mathcal{Y}}_1}^{\mathbf{k}})^{(2)}\} = R_2^k, \ \operatorname{rank}\{(\mathbf{P}_{\boldsymbol{\mathcal{Y}}_3}^{\mathbf{k}})^{(3)}\} = R_3^k, \tag{23}$$

then there exists only one $\widehat{\boldsymbol{\mathcal{P}}}_{\boldsymbol{\mathcal{X}}}^k$ with multilinear ranks at most (R_1^k, R_2^k, R_3^k) that satisties (10)–(14).

Proof. First, by Equation (23), the rank of the unfoldings do not drop after degradation, hence

$$\widehat{\mathbf{U}}^k = \mathbf{U}^k \mathbf{Q}_U, \ \widehat{\mathbf{V}}^k = \mathbf{V}^k \mathbf{Q}_V, \ \widehat{\mathbf{W}}^k = \mathbf{W}^k \mathbf{Q}_W,$$

where $\mathbf{Q}_U, \mathbf{Q}_V, \mathbf{Q}_W$ are some rotation matrices.

Then, let us note that problem (20) can be solved through normal equations of the form

$$\left(\mathbf{X}^\mathsf{T}\mathbf{X}\right) \boldsymbol{g}^k = \mathbf{X}^\mathsf{T}\boldsymbol{z},$$

where the matrix on the left-hand side is

$$\mathbf{X}^\mathsf{T}\mathbf{X} = \mathbf{I}_{R_3^k} \boxtimes \widehat{\mathbf{V}}^{k\mathsf{T}} \mathbf{D}_3^\mathsf{T} \mathbf{D}_3 \widehat{\mathbf{V}}^k \boxtimes \mathbf{I}_{R_1^k}$$

and the vector on the right-hand side is

$$\mathbf{X}^\mathsf{T}\boldsymbol{z} = \operatorname{vec}\{[\![\boldsymbol{\mathcal{P}}_{\boldsymbol{\mathcal{Y}}_3}^k; \widehat{\mathbf{U}}^{k\mathsf{T}}, \widehat{\mathbf{V}}^{k\mathsf{T}} \mathbf{D}_3^\mathsf{T}, \widehat{\mathbf{W}}^{k\mathsf{T}}]\!]\}.$$

Therefore the reconstructed subtensor of $\boldsymbol{\mathcal{X}}$ can be written as

$$\operatorname{vec}\{\widehat{\boldsymbol{\mathcal{P}}}_{\boldsymbol{\mathcal{X}}}^k\} = \left(\widehat{\mathbf{W}}^k \boxtimes \widehat{\mathbf{V}}^k \boxtimes \widehat{\mathbf{U}}^k\right) \left(\mathbf{X}^\mathsf{T}\mathbf{X}\right)^{-1} \mathbf{X}^\mathsf{T}\boldsymbol{z},$$

and does not depend on the rotation matrices $\mathbf{Q}_U, \ \mathbf{Q}_V, \ \mathbf{Q}_W$. Hence the reconstructed tensor $\widehat{\boldsymbol{\mathcal{P}}}_{\boldsymbol{\mathcal{X}}}^k$ is unique. □

Corollary V.2. *If the conditions of Theorem V.1 hold, then Algorithm 2 recovers the K subtensors of $\boldsymbol{\mathcal{X}}$ of the form*

$$\widehat{\boldsymbol{\mathcal{P}}}_{\boldsymbol{\mathcal{X}}}^k = [\![\boldsymbol{\mathcal{G}}^k; \widehat{\mathbf{U}}^k, \widehat{\mathbf{V}}^k, \widehat{\mathbf{W}}^k]\!] \ \forall k \in \{1, \ldots, K\}.$$

Indeed, according to [26, Theorem 5], the MLP method is guaranteed to recover the sparse signal $\boldsymbol{g}^k$ when solving (20) under constraints (19) in the noiseless case.

B. Generic recovery conditions

From the deterministic results, the following generic conditions can be established, *i.e.*, they hold for any generic tensor.

Theorem V.3. *Assume that $\mathbf{D}_1 \in \mathbb{R}^{x_1 \times x}$, $\mathbf{D}_2 \in \mathbb{R}^{y_2 \times y}$, and $\mathbf{D}_3 \in \mathbb{R}^{s_3 \times s}$ are fixed full row-rank matrices. Let $\boldsymbol{\mathcal{P}}_{\boldsymbol{\mathcal{X}}}^k$ admit a Tucker decomposition as in Equation* (9), *where $\boldsymbol{\mathcal{G}} \in \mathbb{R}^{R_1^k \times R_2^k \times R_3^k}$, $R_1^k \leqslant x$, $R_2^k \leqslant y$, $R_3^k \leqslant s$, and $\mathbf{U}^k \in \mathbb{R}^{p^2 \times R_1^k}$, $\mathbf{V}^k \in \mathbb{R}^{s \times R_2^k}$, $\mathbf{W}^k \in \mathbb{R}^{n_k \times R_3^k}$ are random tensor and matrices, distributed according to an absolutely continuous probability distribution. We also assume that $\boldsymbol{\mathcal{E}}_i = \mathbf{0}$ $(i = 1, 2, 3)$ in* (4).

If

$$R_1^k \leqslant p^2 \text{ and } R_2^k \leqslant s_3 \text{ and } R_3^k \leqslant n_k, \tag{24}$$

then with probability 1 *there exists only one* $\boldsymbol{\mathcal{P}}^k_{\boldsymbol{\mathcal{X}}}$ *with multilinear ranks at most* (R_1^k, R_2^k, R_3^k) *such that satisfies* (4).

Proof. First, the conditions on R_1^k and R_3^k fall from the proof for Theorem V.1 and are offered by the semi-blind estimation strategy that we proposed.

Second, let us explain the condition on R_2^k. Without loss of generality, $\mathbf{D}_3$ can be replaced with $\mathbf{D}_3 = [\mathbf{I}_{s_3}\ \mathbf{0}]$. Indeed, there exists a non-singular matrix $\mathbf{T}$ such that $\mathbf{D}_3\mathbf{T} = [\mathbf{I}_{s_3}\ \mathbf{0}]$. If we take $\widetilde{\mathbf{V}}^k = \mathbf{T}^{-1}\mathbf{V}^k$ then $\mathbf{D}_3\mathbf{V}^k = \mathbf{D}_3\widetilde{\mathbf{V}}^k$. A nonsingular transformation preserves absolute continuity of the distribution; hence $\mathbf{V}^k$ has an absolutely continuous distribution if and only if $\widetilde{\mathbf{V}}^k$ has one.

Therefore under the assumption on the distribution of $\mathbf{V}^k$, the following hold with probability 1:

$$R_3^k \leqslant s_3 \Rightarrow \operatorname{rank}\{\mathbf{V}^k_{1:s_3,:}\} = R_3^k.$$

□

Remark V.4. *In the special case where the observations are not partitioned (*i.e., $p = x = y$ *and* $M_x = M_y = 1$ *and* $K = 1$*), then the conditions* (24) *in Theorem V.3 become*

$$R_1^k \leqslant x \text{ and } R_2^k \leqslant y \text{ and } R_3^k \leqslant s_3. \tag{25}$$

VI. METHODS

All simulations were run on a MacBook Pro with 2.3 GHz Intel Core i5 and 16GB RAM. The code was implemented in MATLAB. For tensor operations we used TensorLab 3.0 [28]. The code is available online at https://cprevost4.github.io/RICOTTA_Software/.

A. Experiments setup

Image reconstruction is usually performed from LRIs with arbitrary orientations (*i.e.*, with non-strictly orthogonal views). In this setting, solving the reconstruction problem requires an accurate knowledge of patient position and modality configuration to avoid any alignment errors. Compared to the previously published work, here a preprocessing step was applied in order to cast the acquired data and observation model into the separable form given in Equation (4). This consisted of a resampling, as in the native image space, degradation occurs in the slice direction. Generally, MRI scans may not be strictly orthogonal, so a rigid transformation (3D rotation and translation) was applied to the 3D images. This information was extracted from the native images' DICOM file headers as recorded by the imaging system.

Algorithm 2 was compared to several baseline algorithms. Two geometrical super-resolution (SR) algorithms were considered, with Tikhonov (SR$_T$) and Beltrami (SR$_B$) regularization [8]. The performance of RICOTTA [18], that uses a global tensor low-rank approximation to reconstruct the image, was also assessed. The hyperparameters for these methods were tuned according to the original works.

B. Validation

To evaluate the quality of the reconstructed images $\widehat{\boldsymbol{\mathcal{X}}}$, several quantitative metrics [29] were considered. The first one was the peak signal to noise ratio (PSNR), defined as

$$\text{PSNR} = \frac{10}{s}\sum_{k=1}^{s}\log_{10}\left(\frac{xy\mathbb{E}\left\{(\boldsymbol{\mathcal{X}})_{:,:,k}\right\}}{\|(\boldsymbol{\mathcal{X}})_{:,:,k} - (\widehat{\boldsymbol{\mathcal{X}}})_{:,:,k}\|_F^2}\right), \tag{26}$$

where $\mathbb{E}\{\cdot\}$ denoted the expectation operator.

The second metric was the root mean-squared error

$$\text{RMSE} = \frac{\|\boldsymbol{\mathcal{X}} - \widehat{\boldsymbol{\mathcal{X}}}\|_F^2}{\|\boldsymbol{\mathcal{X}}\|_F^2}. \tag{27}$$

The third one was the Cross-Correlation (CC), taking values between 0 and 1:

$$\text{CC} = \frac{1}{xys}\left(\sum_{k=1}^{s}\rho\left(\boldsymbol{\mathcal{X}}_{:,:,k}, \widehat{\boldsymbol{\mathcal{X}}}_{:,:,k}\right)\right), \tag{28}$$

where $\rho(\cdot,\cdot)$ is the Pearson correlation coefficient between the estimated and original slices.

Then, the Structural Similarity Index Measure (SSIM), used to measure the structural differences between $\boldsymbol{\mathcal{X}}$ and $\widehat{\boldsymbol{\mathcal{X}}}$ [30], was computed.

The average sharpness index (SI) [31], widely used for automatic image restoration and image quality assessment without reference, was calculated across the two first spatial dimensions (namely SI$_x$, SI$_y$) and the average SI across the frontal slice dimension (denoted SI$_s$). The computational time in seconds for each algorithm was given by the `tic` and `toc` functions of MATLAB.

C. Datasets

1) Phantom data: A test object (physical phantom), used for quality control and resolution assessment, was scanned with a 3T Prisma MRI scanner (Siemens Healthineers, Erlangen, Germany). The HRII was obtained and was used as the reference for comparison of the different SR reconstruction methods. The acquisition used a turbo spin echo sequence, with a native resolution of $1 \times 1 \times 1.1$ mm^3 (1.1 mm was the finest resolution allowed by the scanner here), which was interpolated to $1 \times 1 \times 1$ mm^3 and zero-padded in the third dimension to produce a reference tensor $\boldsymbol{\mathcal{X}} \in \mathbb{R}^{224\times224\times224}$, considered as the ground truth image (HRII). The scan time for the HRII was 6 min and 30 s.

Low-resolution scans (observed LRI data) were acquired in three orthogonal orientations with voxels of size $1 \times 1 \times 4$ mm^3 in each of the three orientations. The three observations were such that $\boldsymbol{\mathcal{Y}}_1 \in \mathbb{R}^{56\times224\times224}$, $\boldsymbol{\mathcal{Y}}_2 \in \mathbb{R}^{224\times56\times224}$ and $\boldsymbol{\mathcal{Y}}_3 \in \mathbb{R}^{224\times224\times56}$, respectively. Thus the downsampling ratio between the HRII and the LRI was $d = 4$. The degradation matrices were such that $\mathbf{D}_1 = \mathbf{D}_2 = \mathbf{D}_3 \in \mathbb{R}^{56\times224}$. The acquisition of each LRI took approximately 2 min.

Secondly, the brain LRI data were acquired with voxels of size $1\times1\times8$ mm^3. The downsampling ratio between the HRII and the LRI was $d = 8$, yielding $\mathbf{D}_1 = \mathbf{D}_2 = \mathbf{D}_3 \in \mathbb{R}^{28\times224}$. The acquisition of each of the three LRI in that case took approximately 1 min.

2) Real brain data: The volunteer experiment was conducted on a 3T Signa HDxt MRI scanner (General Electric, Milwaukee, USA). The volunteer study was approved by an ethics committee and written informed consent was obtained (ClinicalTrials.gov identifier: NCT02887053).

A high-resolution reference dataset of the whole brain (HRII) was acquired using a fast gradient echo sequence with a native resolution of $1 \times 1 \times 1$ mm^3, which was zero-padded in the third dimension to produce a reference tensor $\boldsymbol{\mathcal{X}} \in \mathbb{R}^{224\times224\times224}$, considered as the ground-truth HRII. The scan time for the HRII was 8 min. Brain LRI data were obtained with voxels of size $1 \times 1 \times 4$ mm^3 ($d = 4$). The acquisition of each LRI took approximately 2 min.

An additional LRI dataset was acquired, to push the scanner resolution limit, with voxel of size $0.5 \times 0.5 \times 2$ mm^3 (the total scan time was 11 min). Here the 3 volumes were placed such that their intersection covered the cerebellum region, and the SR reconstruction aimed at $0.5 \times 0.5 \times 0.5$ mm^3, which was significantly below the typical resolution of clinical brain scans on a 3T scanner. For this dataset, due to the scanner limitations, the reference was taken as the reconstruction obtained by Beltrami-based inversion.

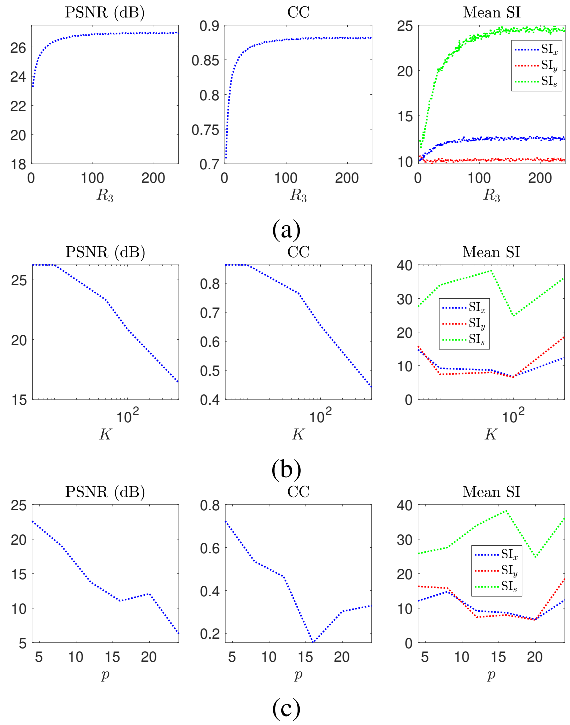

(a)

(b)

(c)

Fig. 2. PSNR, CC and mean SI in three orientations, as a function of : (a) the rank R_3 in the cluster dimension; (b) the number K of different clusters; (c) the size p of the window used to create the subtensors.

Method	PSNR (dB) ↑	SSIM ↑	RMSE ↓	CC ↑	Time (s) ↓	Total time (min, s) ↓
First brain dataset						
Proposed	32.17	0.627	**97.26**	0.967	**117.10**	**7 min 57 s**
RICOTTA	30.46	0.553	131.39	0.923	221.28	9 min 41 s
SR$_T$	20.77	0.699	212.10	**0.986**	224.08	9 min 43 s
SR$_B$	**35.69**	**0.841**	509.09	0.977	130.81	8 min 9 s
Second brain dataset						
Proposed	**28.46**	0.711	**51.38**	**0.936**	10.60	11 min 10 s
RICOTTA	28.26	**0.759**	83.48	0.934	**0.83**	**11 min 1 s**
SR$_T$	13.65	0.571	185.27	0.709	1.07	11 min 1 s
SR$_B$	12.22	0.558	310.81	0.459	5.91	11 min 6 s
First phantom dataset						
Proposed	37.25	0.664	**27.68**	0.998	**97.39**	**7 min 36 s**
RICOTTA	36.85	0.717	29.28	**0.999**	205.83	9 min 24 s
SR$_T$	15.14	0.712	249.28	0.999	209.96	9 min 29 s
SR$_B$	**40.11**	**0.802**	42.44	0.999	165.25	8 min 45 s
Second phantom dataset						
Proposed	**34.70**	0.572	**33.35**	**0.999**	50.73	6 min 51 s
RICOTTA	32.18	**0.600**	41.19	0.999	**13.31**	**6 min 13 s**
SR$_T$	15.52	0.207	206.92	0.963	18.89	6 min 19 s
SR$_B$	20.05	0.229	159.99	0.961	221.81	9 min 41 s

TABLE I

RECONSTRUCTION METRICS, COMPUTATION TIME AND TOTAL PROCESSING TIME.

VII. NUMERICAL RESULTS

A. *Tuning of the parameters*

The good performance of our method relied on the tuning of several hyperparameters. In medical imaging, the best assessment of the image quality is often performed by the practitioner. The hyperparameters were chosen to yield good SI, the closest metric to the human expertise.

For this study, we used the second brain dataset with $x = y = s = 100$. Firstly, the choice of the ranks is usually a very difficult question arising when using tensor factorization. Here, we set $R_1 = p^2$ and $R_2 = s_3$ to avoid artifacts in the reconstructed image dimensions. Figure 2-(a) showed the metrics as a function of $R_3 \in \{1, \dots, \frac{M_x M_y}{K}\}$. They increased with R_3, and reached a plateau around $R_3 = 100$. Hence we set $R_3^k = \min(100, n_k)$ for $k \in \{1, \dots, K\}$.

Figure 2-(b) showed on a semi-log scale the metrics as a function of $K \in \{1, 2, 5, \dots, 100, 200, 500\}$. The PSNR and CC decreased from $K = 10$, while the SI were best for $K = 500$. This is reasonable since a better sharpness means that the pixels are less “blurred”. As a result, we set $K = 100$.

Figure 2-(c) showed the influence of the number of subtensors $p \in \{4, 8, \dots, 24\}$ of the reconstruction. The PSNR and CC decreased with p. The sharpness SI$_x$ and SI$_y$ were rather stable while SI$_s$ was generally higher for a large value of p. It is reasonable since a large value of p might fail to capture the different types of regions in the image. In our other experiments, we took $p = 4$.

B. *Reconstruction performance*

Table Ishowed the reconstruction performance of Algorithm 2 and of the benchmarked algorithms. The best result of each column was shown in bold.

The proposed algorithm yielded most of the best metrics for a large downsampling ratio ($d = 8$). The PSNR and SSIM of the Beltrami-based approach was generally better for $d = 4$, but with a higher runtime. The proposed algorithm had a competitive tradeoff between processing time and reconstruction performance.

Figures 3 to 5 showed greyscale slices of the reference and reconstructed HRII in the three orientations, with a close-up picture on some details. The average SI was indicated for each orientation.

Our approach reconstructed the image correctly. In particular, it provided the best sharpness for the second brain dataset. The Beltrami regularization added during reconstruction of the subtensors corrected artifacts due to the low-rank assumption while preserving the details of the image. The quality of the reconstructed image was similar to that of the reference HRII,

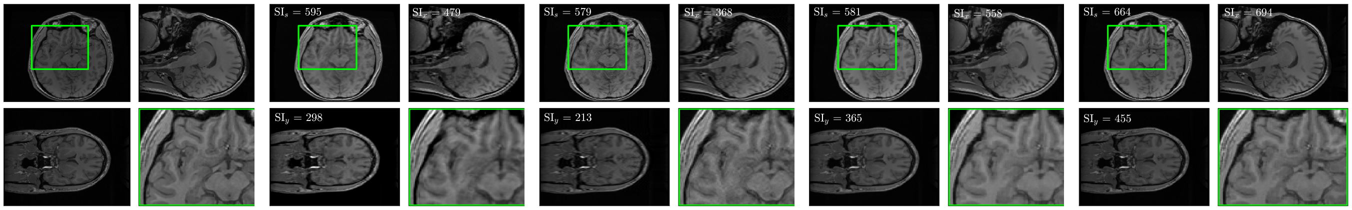

(a) (b) (c) (d) (e)

Fig. 3. Reconstruction of the first brain HRII. (a) Reference HRII, (b) Proposed approach, (c) RICOTTA, (d) SR_T, (e) SR_B.

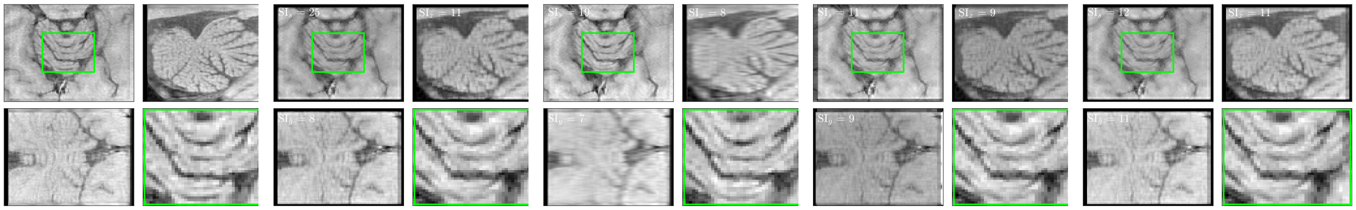

(a) (b) (c) (d) (e)

Fig. 4. Reconstruction of the second brain HRII. (a) Reference HRII, (b) Proposed approach, (c) RICOTTA, (d) SR_T, (e) SR_B.

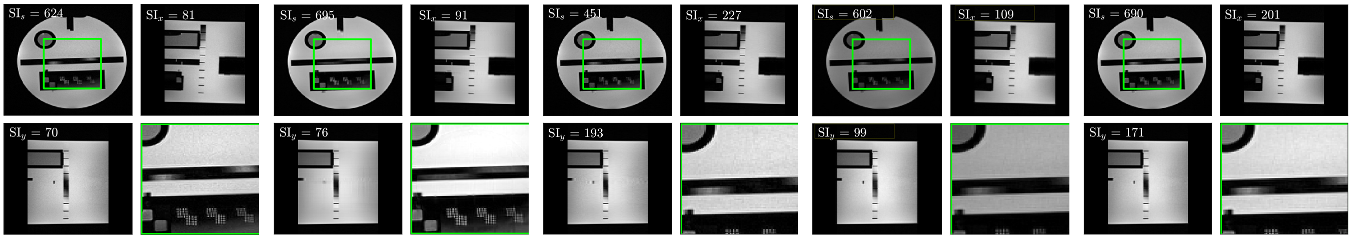

(a) (b) (c) (d) (e)

Fig. 5. Reconstruction of the second phantom HRII. (a) Reference HRII, (b) Proposed approach, (c) RICOTTA, (d) SR_T, (e) SR_B.

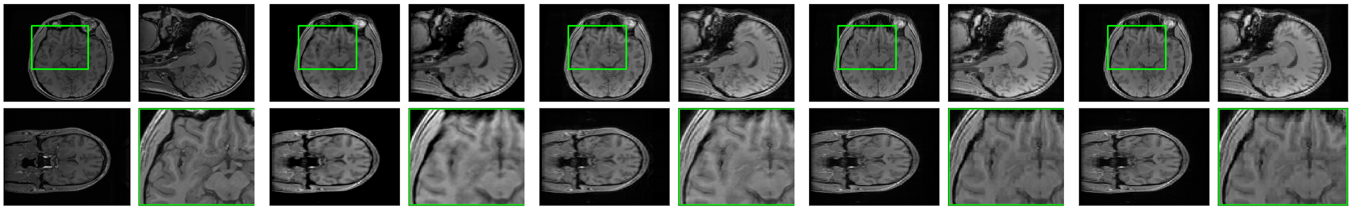

(a) (b) (c) (d) (e)

Fig. 6. Reconstruction of the first brain HRII with two images. (a) Reference HRII, (b) Proposed approach, (c) RICOTTA, (d) SR_T, (e) SR_B.

without the need for a longer acquisition time.

C. *Reconstruction from two images only*

The performance of our method was assessed when using only two LRIs out of three: $\boldsymbol{\mathcal{Y}}_1$ and $\boldsymbol{\mathcal{Y}}_3$ only. Table II showed the reconstruction metrics for the four considered datasets. The best result of each column was shown in bold.

The proposed algorithm slightly higher performance than RICOTTA. It provided the best PSNR and RMSE for all datasets. Its performance was also significantly superior to those of the methods based on regularized model inversion, whose performance highly suffered from the lack of knowledge of one image. The proposed approach was faster than inversion-based methods, especially for the second brain dataset (cerebellum) and second phantom.

Figures 6 to 8 showed greyscale slices of the reference and reconstructed HRII in the three orientations, with zoomed details. Our approach reconstructed the image correctly with a quality similar to that of the reference HRII, without the need for a longer acquisition time. It is also less sensitive to artifacts and loss of quality when using only two images, compared to the baseline approaches.

VIII. CONCLUSION

This paper shows the capabilities of our approach to perform correctly the multi-frame super-resolution task in MRI. Non-local low-rank approximations overcame the difficulties previ-

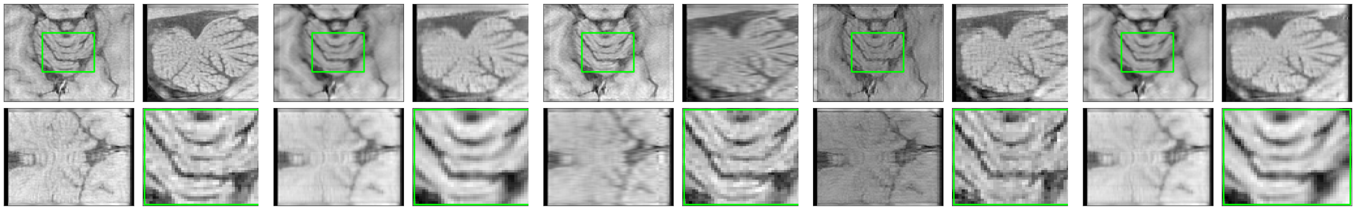

(a) (b) (c) (d) (e)

Fig. 7. Reconstruction of the second brain HRII with two images. (a) Reference HRII, (b) Proposed approach, (c) RICOTTA, (d) SR_T, (e) SR_B.

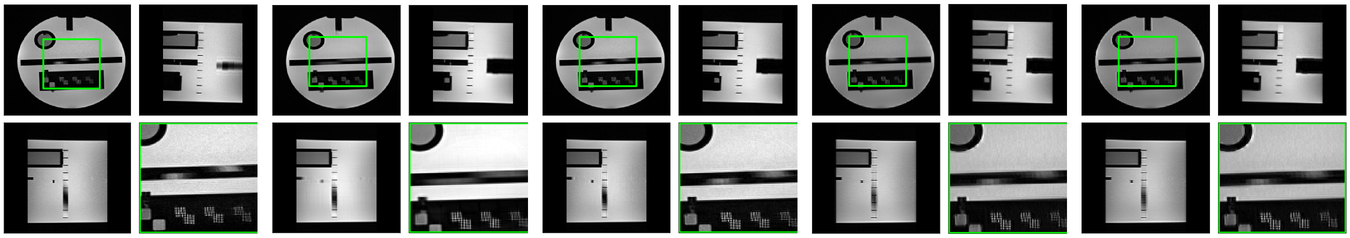

(a) (b) (c) (d) (e)

Fig. 8. Reconstruction of the first phantom HRII with two images. (a) Reference HRII, (b) Proposed approach, (c) RICOTTA, (d) SR_T, (e) SR_B.

Method	PSNR (dB) ↑	SSIM ↑	RMSE ↓	CC ↑	Time (s) ↓	Total time (min, s) ↓
First brain dataset						
Proposed	**32.14**	**0.631**	**41.15**	0.967	122.19	6 min 1 s
RICOTTA	29.02	0.620	55.76	0.897	210.92	7 min 30 s
SR_T	15.02	0.497	337.60	**0.974**	311.24	9 min 11 s
SR_B	20.34	0.630	509.48	0.961	**111.25**	**5 min 51 s**
Second brain dataset						
Proposed	**28.38**	0.702	**48.35**	**0.936**	**19.40**	**7 min 39 s**
RICOTTA	27.68	**0.740**	82.21	0.928	19.75	**7 min 39 s**
SR_T	9.78	0.646	253.17	0.816	193.71	10 min 33 s
SR_B	8.22	0.623	307.57	0.501	25.88	7 min 45 s
First phantom dataset						
Proposed	**37.09**	0.663	**28.36**	**0.999**	**90.33**	**5 min 30 s**
RICOTTA	34.03	**0.692**	37.41	0.999	257.97	8 min 18 s
SR_T	8.90	0.522	455.55	0.997	93.14	5 min 33 s
SR_B	13.15	0.595	375.71	0.996	130.98	6 min 9 s
Second phantom dataset						
Proposed	**34.15**	0.569	**35.63**	0.997	51.82	2 min 52 s
RICOTTA	29.61	**0.593**	52.87	**0.998**	**11.64**	**2 min 11 s**
SR_T	9.04	0.393	389.89	0.993	54.15	2 min 54 s
SR_B	12.24	0.429	320.87	0.993	154.37	4 min 33 s

TABLE II

RECONSTRUCTION METRICS FROM TWO IMAGES ONLY, COMPUTATION TIME AND TOTAL PROCESSING TIME.

ously arising with the non-local matrix and global tensor approaches. The experiments showed that the proposed method was capable of successfully reconstructing the high-resolution isotropic image with only the use of two observations instead of three. The low computation time was lower than the acquisition time of the reference HRII, which confirmed the interest for other approaches.

Our approach has a high versatility for an easy transfer to different imaging fields. It should be applicable to a wide range of MRI acquisition techniques, *e.g.*, T_1-weighted, T_2-weighted, or diffusion-weighted imaging in the brain. It could help improve the trade-off between scan time, resolution, SNR and contrast in MRI. Indeed, this will facilitate the clinical implementation of our algorithm, allowing physicians to obtain images very quickly after acquisition, with both practical (convergence analysis) and theoretical guarantees (theorems).

APPENDIX A
SOLVING FOR $\widehat{\boldsymbol{\mathcal{G}}}$ IN ALGORITHM 1

In this Appendix, we provide details on how to solve for $\widehat{\boldsymbol{\mathcal{G}}}$ in Step 4 of RICOTTA (see Algorithm 1). It consisted in solving the least-squares problem

$$\underset{\widehat{\boldsymbol{\mathcal{G}}}}{\arg\min} \|\mathbf{A}\operatorname{vec}\{\widehat{\boldsymbol{\mathcal{G}}}\} - \boldsymbol{b}\|_F^2 + \mu\|\operatorname{vec}\{\widehat{\boldsymbol{\mathcal{G}}}\}\|_F^2, \tag{29}$$

with

$$\mathbf{A} = \begin{bmatrix} \sqrt{\lambda_1}\widehat{\mathbf{W}} \boxtimes \hat{\mathbf{V}} \boxtimes \mathbf{D}_1\hat{\mathbf{U}} \\ \sqrt{\lambda_2}\widehat{\mathbf{W}} \boxtimes \mathbf{D}_2\hat{\mathbf{V}} \boxtimes \hat{\mathbf{U}} \\ \sqrt{\lambda_3}\mathbf{D}_3\widehat{\mathbf{W}} \boxtimes \hat{\mathbf{V}} \boxtimes \hat{\mathbf{U}} \end{bmatrix}, \quad \boldsymbol{b} = \begin{bmatrix} \sqrt{\lambda_1}\operatorname{vec}\{\boldsymbol{\mathcal{Y}}_1\} \\ \sqrt{\lambda_2}\operatorname{vec}\{\boldsymbol{\mathcal{Y}}_2\} \\ \sqrt{\lambda_3}\operatorname{vec}\{\boldsymbol{\mathcal{Y}}_3\} \end{bmatrix}. \tag{30}$$

It was solved through normal equations of the form

$$\left(\mathbf{A}^\mathsf{T}\mathbf{A} + \mu\mathbf{I}\right)\operatorname{vec}\{\widehat{\boldsymbol{\mathcal{G}}}\} = \mathbf{A}^\mathsf{T}\boldsymbol{b}, \tag{31}$$

with the left-hand side matrix $\mathbf{A}^\mathsf{T}\mathbf{A} =$

$$\lambda_1\mathbf{I}_{R_2R_3} \boxtimes \left(\hat{\mathbf{U}}^\mathsf{T}\mathbf{D}_1^\mathsf{T}\mathbf{D}_1\hat{\mathbf{U}}\right) + \lambda_3\left(\widehat{\mathbf{W}}^\mathsf{T}\mathbf{D}_3^\mathsf{T}\mathbf{D}_3\widehat{\mathbf{W}}\right) \boxtimes \mathbf{I}_{R_1R_2} + \lambda_2\mathbf{I}_{R_3} \boxtimes \left(\hat{\mathbf{V}}^\mathsf{T}\mathbf{D}_2^\mathsf{T}\mathbf{D}_2\hat{\mathbf{V}}\right) \boxtimes \mathbf{I}_{R_1}, \tag{32}$$

and the vector on the right-hand side was $\mathbf{A}^\mathsf{T}\mathbf{b} =$

$$\begin{aligned} &\lambda_1\operatorname{vec}\{[\![\boldsymbol{\mathcal{Y}}_1;\ \hat{\mathbf{U}}^\mathsf{T}\mathbf{D}_1^\mathsf{T}, \hat{\mathbf{V}}^\mathsf{T}, \widehat{\mathbf{W}}^\mathsf{T}]\!]\} \\ &+ \lambda_2\operatorname{vec}\{[\![\boldsymbol{\mathcal{Y}}_2;\ \hat{\mathbf{U}}^\mathsf{T}, \hat{\mathbf{V}}^\mathsf{T}\mathbf{D}_2^\mathsf{T}, \widehat{\mathbf{W}}^\mathsf{T}]\!]\} \\ &+ \lambda_3\operatorname{vec}\{[\![\boldsymbol{\mathcal{Y}}_3;\ \hat{\mathbf{U}}^\mathsf{T}, \hat{\mathbf{V}}^\mathsf{T}, \widehat{\mathbf{W}}^\mathsf{T}\mathbf{D}_3^\mathsf{T}]\!]\}. \end{aligned} \tag{33}$$

Equation (31) was a generalized Sylvester equation:

$$\mathbf{M}_1\widehat{\mathbf{G}}\mathbf{M}_2 + \mathbf{M}_3\widehat{\mathbf{G}}\mathbf{M}_4 = \mathbf{M}_5, \tag{34}$$

where $\widehat{\mathbf{G}}$ was an unfolding of $\widehat{\boldsymbol{\mathcal{G}}}$.

Two options were proposed for converting Equation (31) into Equation (34). In the first case, $\widehat{\mathbf{G}} = \boldsymbol{\mathcal{G}}^{(1)\mathsf{T}} \in \mathbb{R}^{R_1 \times R_2R_3}$,

$$\mathbf{M}_1 = \lambda_1\left(\mathbf{U}^\mathsf{T}\mathbf{D}_1^\mathsf{T}\mathbf{D}_1\mathbf{U}\right), \quad \mathbf{M}_2 = \mathbf{I}_{R_2R_3}, \quad \mathbf{M}_3 = \mathbf{I}_{R_1},$$
$$\mathbf{M}_4 = \lambda_2\left(\mathbf{V}^\mathsf{T}\mathbf{D}_2^\mathsf{T}\mathbf{D}_2\mathbf{V}\right) + \lambda_3\left(\mathbf{W}^\mathsf{T}\mathbf{D}_3^\mathsf{T}\mathbf{D}_3\mathbf{W}\right),$$

and $\mathbf{M}_5 \in \mathbb{R}^{R_2 R_3 \times R_1}$ was a matricization of $\mathbf{A}^\top \boldsymbol{b}$.

In the second case, $\widehat{\mathbf{G}} = \boldsymbol{\mathcal{G}}^{(3)} \in \mathbb{R}^{R_1 R_2 \times R_3}$,

$$\mathbf{M}_1 = \lambda_1 \left(\mathbf{U}^\top \mathbf{D}_1^\top \mathbf{D}_1 \mathbf{U}\right) + \lambda_2 \left(\mathbf{V}^\top \mathbf{D}_2^\top \mathbf{D}_2 \mathbf{V}\right),$$
$$\mathbf{M}_2 = \mathbf{I}_{R_3}, \quad \mathbf{M}_3 = \mathbf{I}_{R_1 R_2}, \quad \mathbf{M}_4 = \lambda_3 \left(\mathbf{W}^\top \mathbf{D}_3^\top \mathbf{D}_3 \mathbf{W}\right),$$

and $\mathbf{M}_5 \in \mathbb{R}^{R_1 R_2 \times R_3}$ is a matricization of $\mathbf{X}^\top \boldsymbol{z}$.

The two options were equivalent and the fastest one was chosen according to the multilinear rank. The complexity for solving equation (34) was thus $O(m^3 + n^3)$ flops for $\widehat{\mathbf{G}} \in \mathbb{R}^{m \times n}$ if fast solvers, such as Hessenberg-Schur or Bartels-Stewart methods [32], were used.

REFERENCES

[1] E. Plenge, D. J. Poot, M. Bernsen, G. Kotek, G. Houston, P. Wielopolski, L. van der Weerd, W. J. Niessen, and E. Meijering, "Super-resolution methods in MRI: Can they improve the trade-off between resolution, signal-to-noise ratio, and acquisition time?," *Magnetic Resonance in Medicine*, vol. 68, no. 6, pp. 1983–1993, 2012.

[2] M. Delbany, A. Bustin, J. Poujol, I. Thomassin-Naggara, J. Felblinger, P.-A. Vuissoz, and F. Odille, "One-millimeter isotropic breast diffusion-weighted imaging: Evaluation of a superresolution strategy in terms of signal-to-noise ratio, sharpness and apparent diffusion coefficient," *Magnetic Resonance in Medicine*, vol. 81, no. 4, 2019.

[3] O. Oktay, W. Bai, M. Lee, R. Guerrero, K. Kamnitsas, J. Caballero, A. de Marvao, S. Cook, D. O'Regan, and D. Rueckert, "Multi-input Cardiac Image Super-Resolution Using Convolutional Neural Networks," in *Medical Image Computing and Computer-Assisted Intervention*, MICCAI 2016, Ed., Cham, 2016, Lecture Notes in Computer Science, pp. 246–254, Springer International Publishing.

[4] J. Shi, Z. Li, S. Ying, C. Wang, Q. Liu, Q. Zhang, and P. Yan, "MR Image Super-Resolution via Wide Residual Networks With Fixed Skip Connection," *IEEE Journal of Biomedical and Health Informatics*, vol. 23, no. 3, pp. 1129–1140, May 2019.

[5] A. Gholipour, J.A. Estroff, and S.K. Warfield, "Robust Super-Resolution Volume Reconstruction From Slice Acquisitions: Application to Fetal Brain MRI," *IEEE Transactions on Medical Imaging*, vol. 29, no. 10, pp. 1739–1758, Oct. 2010.

[6] X. Zhang, E. Y. Lam, E. X. Wu, and K. Y. Wong, "Application of Tikhonov Regularization to Super-Resolution Reconstruction of Brain MRI Images," in *Medical Imaging and Informatics*, Xiaohong Gao, Henning Müller, Martin J. Loomes, Richard Comley, and Shuqian Luo, Eds., number 4987 in Lecture Notes in Computer Science, pp. 51–56. Springer Berlin Heidelberg, 2008.

[7] S. Tourbier, X. Bresson, P. Hagmann, J.-P. Thiran, R. Meuli, and M. B. Cuadra, "Efficient total variation algorithm for fetal brain MRI reconstruction," *Medical image computing and computer-assisted intervention: MICCAI ... International Conference on Medical Image Computing and Computer-Assisted Intervention*, vol. 17, no. Pt 2, pp. 252–259, 2014.

[8] F. Odille, A. Bustin, B. Chen, P.-A. Vuissoz, and J. Felblinger, "Motion-corrected, super-resolution reconstruction for high-resolution 3d cardiac cine mri," in *International Conference on Medical Image Computing and Computer-Assisted Intervention*. Springer, 2015, pp. 435–442.

[9] F. Shi, J. Cheng, L. Wang, P.-T. Yap, and D. Shen, "LRTV: MR Image Super-Resolution with Low-Rank and Total Variation Regularizations," *IEEE transactions on medical imaging*, vol. 34, no. 12, pp. 2459–2466, Dec. 2015.

[10] A. Bustin, D. Voilliot, A. Menini, J. Felblinger, C. de Chillou, D. Burschka, L. Bonnemains, and F. Odille, "Isotropic Reconstruction of MR Images Using 3D Patch-Based Self-Similarity Learning," *IEEE transactions on medical imaging*, vol. 37, no. 8, pp. 1932–1942, Aug. 2018.

[11] B. Zhao, K. Setsompop, E. Adalsteinsson, B. Gagoski, H. Ye, D. Ma, Y. Jiang, Ellen G., M. Griswold, and L. Wald, "Improved MR fingerprinting reconstruction with low-rank and subspace modeling," *Magnetic resonance in medicine*, vol. 79, no. 2, pp. 933–942, 2018.

[12] S. Guo, J. A. Fessler, and D. C. Noll, "High-resolution oscillating steady-state fmri using patch-tensor low-rank reconstruction," *IEEE transactions on medical imaging*, vol. 39, no. 12, pp. 4357–4368, 2020.

[13] A. G. Christodoulou, J. L. Shaw, C. Nguyen, Q. Yang, Y/ Xie, N. Wang, and D. Li, "Magnetic resonance multitasking for motion-resolved quantitative cardiovascular imaging," *Nature biomedical engineering*, vol. 2, no. 4, pp. 215–226, 2018.

[14] B. Yaman, S. Weingärtner, N. Kargas, N. D. Sidiropoulos, and M. Akçakaya, "Low-rank tensor models for improved multidimensional mri: Application to dynamic cardiac t_1 mapping," *IEEE transactions on computational imaging*, vol. 6, pp. 194–207, 2019.

[15] C. I. Kanatsoulis, X. Fu, N. D. Sidiropoulos, and M. Akçakaya, "Tensor Completion from Regular Sub-Nyquist Samples," *arXiv e-prints*, p. arXiv:1903.00435, Mar. 2019.

[16] Z. He, B. Zhao, and Z. Zhang, "Active sampling for accelerated mri with low-rank tensors," in *2022 44th Annual International Conference of the IEEE Engineering in Medicine & Biology Society (EMBC)*. IEEE, 2022, pp. 3024–3028.

[17] M. Akcakaya, M. I. Doneva, and C. Prieto, *Magnetic Resonance Image Reconstruction: Theory, Methods, and Applications*, Elsevier Science & Technology, 2022.

[18] C. Prévost and F Odille, "Multi-frame super-resolution mri using coupled low-rank tucker approximation," in *2022 30th European Signal Processing Conference (EUSIPCO)*. IEEE, 2022, pp. 1263–1267.

[19] H. Jia, X. Chen, Z. Han, B. Liu, T. Wen, and Y. Tang, "Nonconvex nonlocal tucker decomposition for 3d medical image super-resolution," *Frontiers in Neuroinformatics*, vol. 16, 2022.

[20] C. Prévost and F Odille, "Super-resolution reconstruction of brain 3d magnetic resonance images using a coupled tensor multilinear approximation," 2022.

[21] P. Comon, "Tensors: A brief introduction," *IEEE Signal Process. Mag.*, vol. 31, no. 3, pp. 44–53, 2014.

[22] G. H. Golub, P. C. Hansen, and D. P. O'Leary, "Tikhonov regularization and total least squares," *SIAM journal on matrix analysis and applications*, vol. 21, no. 1, pp. 185–194, 1999.

[23] D. Arthur and S. Vassilvitskii, "K-means++ the advantages of careful seeding," in *Proceedings of the eighteenth annual ACM-SIAM symposium on Discrete algorithms*, 2007, pp. 1027–1035.

[24] L. N. Smith and M. Elad, "Improving dictionary learning: Multiple dictionary updates and coefficient reuse," *IEEE Signal Processing Letters*, vol. 20, no. 1, pp. 79–82, 2012.

[25] M. Elad, M. A. Figueiredo, and Y. Ma, "On the role of sparse and redundant representations in image processing," *Proceedings of the IEEE*, vol. 98, no. 6, pp. 972–982, 2010.

[26] M. Tan, I. W. Tsang, and L. Wang, "Matching pursuit lasso part i: Sparse recovery over big dictionary," *IEEE Transactions on Signal Processing*, vol. 63, no. 3, pp. 727–741, 2014.

[27] D. Zosso and A. Bustin, "A primal-dual projected gradient algorithm for efficient beltrami regularization," *Computer Vision and Image Understanding*, pp. 14–52, 2014.

[28] N. Vervliet, O. Debals, L. Sorber, M. Van Barel, and L. De Lathauwer, *Tensorlab 3.0*, Available online, 2016.

[29] W. Pei, G. Wang, and X. Yu, "Performance evaluation of different references based image fusion quality metrics for quality assessment of remote sensing image fusion," in *2012 IEEE International Geoscience and Remote Sensing Symposium*. IEEE, 2012, pp. 2280–2283.

[30] Z. Wang, A. C. Bovik, H. R. Sheikh, and E. P. Simoncelli, "Image quality assessment: from error visibility to structural similarity," *IEEE transactions on image processing*, vol. 13, no. 4, pp. 600–612, 2004.

[31] G. Blanchet and L. Moisan, "An explicit sharpness index related to global phase coherence," in *2012 IEEE International Conference on Acoustics, Speech and Signal Processing*. IEEE, 2012, pp. 1065–1068.

[32] V. Simoncini, "Computational methods for linear matrix equations," *SIAM Review*, vol. 58, no. 3, pp. 377–441, 2016.